74

Predicting the Emissions and Performance Characteristics of a Wankel Engine

Guido A. Danieli, Colin R. Ferguson, John B. Heywood, and James C. Keck

Department of Mechanical Engineering,
Massachusetts Institute of Technology

SOCIETY OF AUTOMOTIVE ENGINEERS

PREDICTING THE EMISSIONS AND
PERFORMANCE CHARACTERISTICS OF A WANKEL ENGINE

Guido A. Danieli, Colin R. Ferguson, John B. Heywood, and James C. Keck

ERRATA

Page 3, Equation (17). Delete second "x =" on left side of equation, i.e.

$$x = \frac{PV - PV_o + (Q + W + H)(\gamma_b - 1)}{c_{v_u}(\gamma_b - \gamma_u)\bar{T}_u m - \Delta H(\gamma_b - 1)m}$$

$$+ \frac{(\gamma_b - \gamma_u)c_{v_u}(m\bar{T}_u - m_o T_o)}{c_{v_u}(\gamma_b - \gamma_u)\bar{T}_u m - \Delta H(\gamma_b - 1)m}$$

$$- \frac{\Delta H(\gamma_b - 1)\langle m - m^* \rangle^o}{c_{v_u}(\gamma_b - \gamma_u)\bar{T}_u m - \Delta H(\gamma_b - 1)m}$$

Page 4, Equations (23) and (24). Left side of each equation should read:

$$\frac{\dot{m}_{jk}}{m_j} =$$

Page 14, Equation (A-1) should read:

$$C_d A = \frac{\left[\frac{(\gamma - 1)}{P}\frac{dQ}{dt} - \frac{d(\ln PV^\gamma)}{dt}\right]}{\sqrt{\gamma RT}\left(\frac{2}{\gamma + 1}\right)^{(\gamma + 1)/2(\gamma - 1)}}$$

Predicting the Emissions and Performance Characteristics of a Wankel Engine

Guido A. Danieli, Colin R. Ferguson, John B. Heywood, and James C. Keck

Department of Mechanical Engineering,
Massachusetts Institute of Technology

THE MECHANISMS of pollutant formation in reciprocating carbureted spark-ignition engines are now understood in principle. A number of mathematical models of nitric oxide (NO) and carbon monoxide (CO) formation have been formulated and experimentally verified for such piston engines. Generally, these emissions models also incorporate an engine performance model. It is well known that NO formation and decomposition are kinetically controlled and that engine NO emissions are dependent upon the temperature-time history and stoichiometry of the bulk burned gases. CO emissions are controlled primarily by stoichiometry of the bulk gases for fuel-rich engine operation, and by the freezing of the CO oxidation process in the bulk gases during expansion and exhaust for fuel-lean operation. In contrast, HC emissions come from the unburned mixture left by the flame quenching at the walls of the combustion chamber. These mechanisms are reviewed in the literature (1,2)*.

These piston engine models, with suitable modifications, should be able to predict the performance and emission characteristics of a Wankel engine. There are several important

*Numbers in parentheses designate References at end of paper.

differences which make the analysis more complicated. Our study is a step in the development of suitable models for the Wankel engine.

The Wankel differs from the conventional engine thermodynamically and geometrically. The Wankel features rotating combustion chambers, gas leakage past the seals couples events in different chambers, and the engine has different shaped combustion chambers with large surface to volume ratios. These primary differences manifest themselves as emissions and performance differences. The Wankel is lower in NO emissions but higher in hydrocarbon (HC) emissions. The exhaust is easier to clean by thermal reaction but the current Wankel has a lower thermal efficiency. A quantitative understanding of the Wankel's performance and emission characteristics has not yet been demonstrated.

The engine has been well described kinematically by Ansdale (4). Sirignano and Bracco (5) have formulated a one-dimensional model of Wankel combustion. The geometry of the combustion chamber has been modeled, but gas leakage has been neglected. Eberle and Klomp (6) have evaluated potential performance gains to be realized through leakage reduction. The purpose of this paper is to develop the relations coupling the mass fraction burned to the chamber pressure and

ABSTRACT

A performance model of a Wankel engine is developed which performs a leakage mass balance, accounts for heat transfer and flame quenching, and predicts the mass fraction burned as a function of chamber pressure. Experiments were performed on a production Wankel engine to obtain chamber pressure-time diagrams, and engine performance and emissions data.

Model predictions of mass burned, global heat transfer, and hydrocarbon emission gave good agreement with measurements. Predictions of oxides of nitrogen are higher than measurements, especially at low loads. This is thought to be due to the adiabatic core gas assumption in the model. The need for a Wankel boundary layer study is identified.

2

to quantify by way of mathematical formulation and experimental verification the engine's performance and NO and HC emission characteristics.

A thermodynamic model of the Wankel is developed and applied to a Toyo Kogyo series 10A production engine. From measured pressure versus time curves calculations are made predicting the burned mass fraction as a function of time, global heat loss, average exhaust concentration of NO and HC, and the relative importance of the three sources of HC in the Wankel—crevice volumes, quenching, and gas leakage. Calculations are also made of the residual mass fraction. A series of experiments was run in which the concentrations of HC, NO, CO, CO_2, and O_2 in the exhaust were measured. Also measured were the engine's bmep, fmep, fuel flow, air flow, heat loss, and intake manifold pressure.

MODEL DESCRIPTION

The Wankel is modeled such that any given chamber is an open system exchanging mass with both the chamber trailing and the chamber leading the one of interest. Fig. 1 shows a schematic of the control volumes involved. In any given chamber the pressure is assumed uniform and the process quasi-static.

The energy equation for such an open system is

$$\frac{dE}{dt} = -\sum_i h_{s_i} \dot{m}_i - \frac{dW}{dt} - \frac{dQ}{dt} \quad (1)$$

where:

E = energy of system
h_s = specific stagnation enthalpy
$\dot{m}$ = mass flux out of system
W = work done by system
Q = heat loss by system
subscript i = different mass fluxes

In the combusting chamber the energy may be identified as

$$E = mu = \int_0^{m_b} u_b dm + \int_0^{m_u} u_u dm \quad (2)$$

where:

u = specific internal energy
m = mass
subscripts u and b = unburned and burned gases, respectively

Assuming ideal gases, the internal energies may be written as

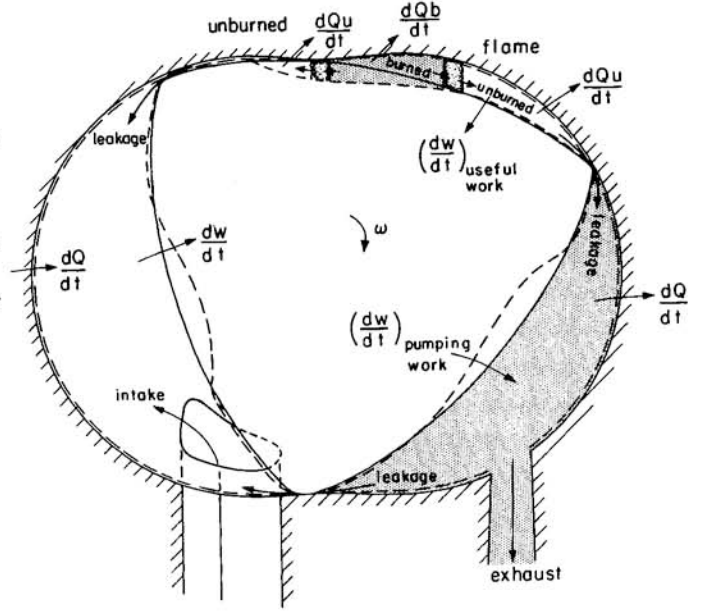$$u = c_v T + h_f^o \quad (3)$$

and enthalpies as

Fig. 1 - Schematic depicting coupling of three control volumes by leakage past apex seals

$$h = c_p T + h_f^o \quad (4)$$

where:

T = temperature
c_v = constant volume specific heat
c_p = constant pressure specific heat
h_f^o = enthalpy of formation at absolute zero

Defining then the burned gas mass fraction

$$x = \frac{m_b}{m} \quad (5)$$

and the average temperatures

$$\overline{T}_u = \frac{1}{1-x} \int_x^1 T_u dx' \quad (6)$$

$$\overline{T}_b = \frac{1}{x} \int_0^x T_b dx' \quad (7)$$

and integrating the energy equation over time using Eqs. 2-7 yields

$$m[(c_{v_b} \overline{T}_b + h_{f_b}^o) x + (c_{v_u} \overline{T}_u + h_{f_u}^o)(1-x)]$$

$$= m_o U_o - \sum_i \int_0^t c_{pi} T_{si} \dot{m}_i dt - \int_0^t dW - \int_0^t dQ \quad (8)$$

where subscript o indicates conditions at some specified reference time.

A mass balance gives

$$m = m_o - \sum_i \int_o^t \dot{m}_i dt \qquad (9)$$

where the $\dot{m}_i$ are calculated as quasi-steady one-dimensional flows according to Eqs. 23 and 24. Since the volume of the flame reaction zone is small, the volume is given by

$$V = \int_o^{m_b} v_b dm + \int_o^{m_u} v_u dm \qquad (10)$$

where:

v = specific volume

The definition of x and the equation of state

$$PV = mRT \qquad (11)$$

then give

$$\frac{PV}{m} = \int_o^x R_b T_b dx' + \int_x^1 R_u T_u dx' \qquad (12)$$

Defining then m* as the mass present in the chamber at the time (t*) when combustion ends, and using the notation

$$H = \int_o^t \sum_i c_{p_i} T_{s_i} \dot{m}_i \, dt \qquad (13)$$

$$Q = \int_o^t dQ \qquad (14)$$

$$W = \int_o^t dW \qquad (15)$$

$$\Delta H = h_{f_b}^o - h_{f_u}^o \qquad (16)$$

the mass fraction of the burned gases for constant specific heats is then given by

$$x = \frac{PV - PV_o + (Q + W + H)(\gamma_b - 1)}{c_{v_u}(\gamma_b - \gamma_u)\overline{T}_u m - \Delta H(\gamma_b - 1)m}$$

$$+ \frac{(\gamma_b - \gamma_u)c_{v_u}(m\overline{T}_u - m_o T_o)}{c_{v_u}(\gamma_b - \gamma_u)\overline{T}_u m - \Delta H(\gamma_b - 1)m}$$

$$x = - \frac{\Delta H(\gamma_b - 1)\langle m - m^* \rangle^o}{c_{v_u}(\gamma_b - \gamma_u)\overline{T}_u m - \Delta H(\gamma_b - 1)m} \qquad (17)$$

where the singularity function $\langle m - m^* \rangle^o$ is zero for all times $t < t^*$. Notice that x so calculated is identical to the one calculated in Ref. 7 when there are no leaks; hence, $m^* = m = m_o$ = constant and H = 0.

Through heat transfer the unburned gas loses energy to the chamber walls and receives energy from the burned gas. The net exchange is such that a reasonable approximation for the average unburned gas temperature is

$$\frac{\overline{T}_u}{T_o} = \left(\frac{P}{P_o}\right)^{\gamma_u - 1/\gamma_u} \qquad (18)$$

The burned mass fraction, as defined in Eq. 17, is evaluated using Eq. 18 and a measured pressure versus time curve. The reference time is chosen to be the time of ignition, and the initial condition required at this time is the unburned temperature estimated according to Eq. 11 based on the mass in the chamber at this time.

The pressure measurement is made with an a-c coupled PCB piezoelectric transducer mounted at the leading spark plug. The pressure trace thus obtained is only for 120 deg of rotor rotation; however, it records the entire combustion and expansion processes.

The three working chambers, identifiable at any given time, are coupled thermodynamically via leakage. Thus, an entire cycle must be mathematically simulated to estimate the mass in the chamber at ignition. Models of the compression, exhaust, and induction strokes are connected and the entire model iterated to obtain self-consistency.

The simulation begins at the instant the intake port closes. The mass in the chamber at this time is composed of the mass inducted per revolution, the residual mass, and leakage from the leading compressing chamber and the trailing exhausting chamber. The mass when the intake port closes is

$$m_{ic} = m_{ind} + m_r + \sum_i \int_{t_{io}}^{t_{ic}} \dot{m}_i dt \qquad (19)$$

where:

r = properties of residual mass
ind = properties of mass inducted per revolution
io = angle at which intake port opens
ic = angle at which intake port closes

Because the inducting chamber always receives leakage, that leakage can be calculated using the measured average induction pressure as the downstream pressures in Eqs. 23 and 24.

For the early part of the compression phase there is no pressure record from the spark plug mounted transducer. The pressures from P_{ic} to the first measured pressure (100 deg btdc) are therefore calculated according to

$$PV^{\gamma_u} = \text{constant} \qquad (20)$$

where the pressure is matched at the volume of the first measured pressure.

To model the exhaust process, the equation of state (Eq. 11) is time differentiated and solved together with the energy equation (Eq. 1) rearranged as follows

$$\frac{1}{P}\frac{dP}{dt} = \frac{1}{T}\frac{dT}{dt} - \frac{1}{V}\frac{dV}{dt} - \frac{\dot{m}_{out}}{m} + \frac{\dot{m}_{in}}{m} \qquad (21)$$

$$\frac{1}{T}\frac{dT}{dt} = (1 - \gamma_E)\left[\frac{1}{PV}\frac{dQ}{dt} + \frac{1}{V}\frac{dV}{dt} + \frac{\dot{m}_{out}}{m}\right] + \frac{\dot{m}_{in}}{m}\left[\frac{c_{p_{in}} T_{s_{in}}}{c_{v_E} T} - 1\right] \qquad (22)$$

where

$\dot{m}_{out}$ = mass flow leaving system

$\dot{m}_{in}$ = mass flow entering system

subscript E = properties of exhaust gas

The derivation of Eqs. 21 and 22 assumes that leakage of unburned fuel and air into the exhaust does not react. In view of the temperatures typical of the exhausting chamber and the fact that we are only analyzing fuel-rich cases, this assumption is expected to be good.

The simultaneous solution of Eqs. 21 and 22 begins at the instant the exhaust port opens. The pressure and temperature at this time (initial conditions) comes from the measured pressure-time curve and the temperature from expansion phase calculations.

Mass fluxes between chambers and through the exhaust port are assumed to be quasi-steady and are calculated according to

$$\frac{m_{jk}}{m_j} = \frac{C_d A_{jk}}{V_j} \sqrt{\gamma_j R_j T_j} \left(\frac{2}{\gamma_j + 1}\right)^{(\gamma_j+1)/2(\gamma_j-1)}:$$

$$\frac{P_j}{P_k} > \left(\frac{\gamma_j + 1}{2}\right)^{\gamma_j/\gamma_j - 1} \qquad (23)$$

$$\frac{m_{jk}}{m_j} = \frac{C_d A_{jk}}{V_j} \sqrt{\gamma_j R_j T_j} \left\{\frac{2}{\gamma_j - 1}\left[\left(\frac{P_k}{P_j}\right)^{2/\gamma_j} - \right.\right.$$

$$\left.\left.\left(\frac{P_k}{P_j}\right)^{(\gamma_j+1)/\gamma_j}\right]\right\}^{1/2} : \frac{P_j}{P_k} \leqslant \left(\frac{\gamma_j + 1}{2}\right)^{\gamma_j/\gamma_j - 1} \qquad (24)$$

where indices j and k denote upstream and downstream conditions respectively, and C_d is the discharge coefficient of the communication area A_{jk}. The upstream conditions truly refer to the stagnation conditions upstream; however, the kinetic energy in any given chamber can be assumed negligible. Therefore the stagnation temperature and pressure of the mass leaving the system are equal to the static upstream temperature and pressure.

The exhaust port was modeled as opening linearly to its full area of $4.84 cm^2$ in 16 crank angle deg. A discharge coefficient of 0.85 was used for the exhaust port. The effective leakage area was taken to be 1 mm^2 following the analysis described in the Appendix.

There is a physical distinction to be made between the inlet charge, which is fuel and air, and the unburned gas. This is handled by keeping track of the dilution of the inlet charge by burned gases which are internally recycled within the engine. A useful number for this purpose is the effective residual mass fraction defined as

$$\epsilon = \frac{m_r + m_{\ell b}}{m_{int} + m_r + m_{\ell b}} \qquad (25)$$

where $m_{\ell b}$ denotes the mass leaked into the inducting chamber from the exhausting chamber. An analogous term, which could be denoted $m_{\ell u}$, of leakage from the compressing chamber into the inducting chamber does not appear since this mass is of the same composition as defined by Eq. 25.

The effective residual mass fraction depends on the aerodynamics around the apex seal as it uncovers the exhaust port. During this time (16 deg) there is communication between the chamber about to begin induction and the chamber blowing down. During the last 3 deg of this time there is an overlap of the intake port and the exhaust port. Two cases are possible—mass may transfer from the exhaust to the chamber about to begin induction or vice versa—depending upon that chamber's pressure and how the choked blowdown makes the required pressure adjustment to the back pressure. One-dimensional estimates indicate that in either case the effect is negligible and consequently it does not appear in Eq. 25.

To calculate the effect of wall quenching, the approximate position of the flame front during the combustion process must be evaluated. Geometrically the burning is modeled as two flames propagating in a box of length and width defined by the rotor dimensions. The height of the box is varied sinusoidally to match the time behavior of the chamber volume. The surface area of this box differs from that of the real engine by about 10%. A corrected formula for surface area A is:

$$\frac{A}{2} = \frac{V}{b} + \frac{V}{L} + bL + C \qquad (26)$$

where:

C = correction factor (accounts for 10% difference)
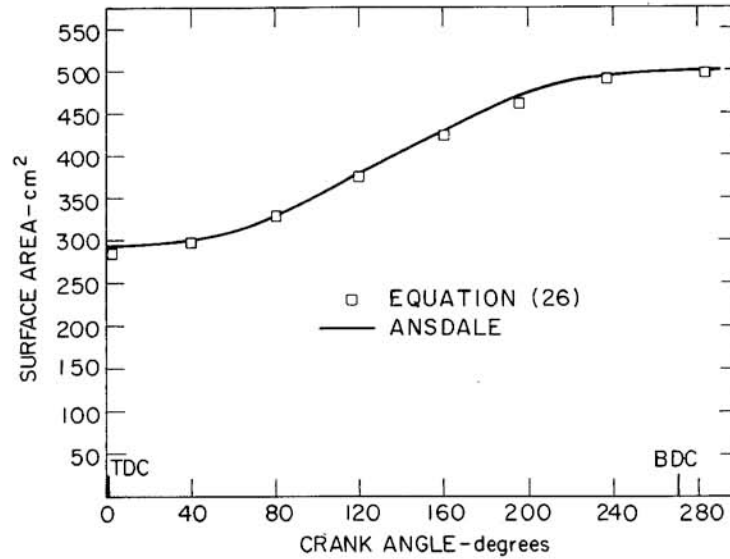b = rotor width
L = rotor length
V = volume

Fig. 2 - Comparison of Eq. 26 to exact method outlined by Ansdale

Fig. 2 shows a comparison between the area calculated according to Eq. 26 and the area calculated via a technique outlined by Ansdale (4). The latter approach requires numerical integration at each time step, the result is shown as the continuous curve, and there is no significant difference.

A unique feature of this model is the manner in which flame quenching enters as a constraint on the mass fraction burned. As the flame propagates through the combustion chamber the quench layer left behind is considered as mass and enthalpy which left the system modeled by Eq. 1. Shown schematically in Fig. 3, the mass quenched in an interval of time δt is assumed to be given by

$$\delta m_q = \frac{PqA}{R_u T_u} \cdot \frac{\delta V_b}{V} \qquad (27)$$

where q is the quench layer's thickness and δV_b is the incremental volume change of the burned gas. With the mass so computed, its enthalpy and volume are removed from the system at every time step and the procedure continued until a stationary value of x is found.

The quench thickness is calculated from

$$\frac{q}{q_{rc}} = 0.4 \left(\frac{P_{rc}}{P}\right)^\alpha \left(\frac{T_{rc}}{T_u}\right)^\beta \qquad (28)$$

where

β = Friedman and Johnston temperature coefficient
α = Agnew and Green pressure coefficient
rc = subscript to denote reference conditions

The reference quench conditions based on data in Ref. 8 are shown in Table 1, as are the pressure and temperature coefficients based on Refs. 9 and 10. The constant 0.4 in Eq. 28
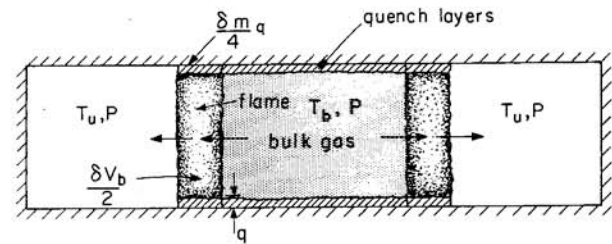

Fig. 3 - Geometrical model of flame quenching

Table 1 - Quenching Parameters as a Function of Equivalence Ratio ϕ

$T_{rc} = 373$ K, $P_{rc} = 4$ atm

ϕ	q_{rc}, mm	β	α
0.90	0.850	0.64	0.53
1.00	0.640	0.50	0.52
1.10	0.564	0.50	0.62
1.20	0.543	0.50	0.66
1.30	0.539	0.50	0.66

adjusts the quench distance to correspond to a single wall quench distance (11).

In a manner analogous to the quenching, mass is removed when it is compressed into the crevice volumes composed of the clearance between the rotor and the side covers, and the distance between the rotor's edge and the first side seal. The crevice volume used in the calculations is 0.122 cm^3 per chamber.

An adequate model of heat transfer in the Wankel has not yet been developed. It is reasonable to expect that energy losses by way of heat transfer are considerable. Not only does the Wankel possess characteristically large surface to volume ratios but also large velocity gradients at stationary surfaces,

since generally the working fluid constrained between apex seals is forced to rotate at the rotor speed.

Dimensional analysis applied to forced convection suggests that the Nusselt number is some function of the Reynolds number and the Prandtl number. Our study uses the correlations due to Woschni (12) primarily because his Nusselt number displayed the expected Reynolds number dependence:

$$Nu = 0.035 \, Re^{0.8} \qquad (29)$$

The constant 0.035 has been checked by comparing measured average heat losses to predicted average heat losses.

The time averaged gas velocity within the Wankel is

$$W_z = \frac{r\omega}{3} \, , \text{m/s} \qquad (30)$$

where:

r = generating radius, m
ω = crankshaft angular velocity, s^{-1}

The factor 3 appears because the rotor rotates at one-third the speed of the crankshaft. In addition, the combustion-induced motion is calculated by Woschni's equation.

$$W_c = 0.00324 \frac{V_d T}{P_o V_o} (P - P_m), \text{m/s} \qquad (31)$$

where:

P = firing pressure, atm
P_m = motoring pressure, atm
V_d = displacement volume, m^3

The total gas velocity may therefore be written

$$W = \frac{r\omega}{3} + 0.00324 \frac{V_d T_o}{P_o V_o} (P - P_m), \text{m/s} \qquad (32)$$

In addition to a gas velocity, the correlation requires a characteristic diameter, which in this study is the hydraulic diameter of the flow passage shown in Fig. 3. In terms of our simplified geometry this is

$$\frac{d}{2} = (1/b + bL/V)^{-1}, \text{m} \qquad (33)$$

Using Woshni's relations for density, viscosity, and thermal conductivity, Eq. 29 may be solved for the heat transfer coefficient and yields

$$H = 110 \, d^{-0.2} \, P^{0.8} \, T^{-0.53} \, W^{0.8}, \text{kcal/m}^2/\text{h/K} \qquad (34)$$

where d is in metres, P in atmospheres, T in degrees Kelvin, and W in metres/second.

The heat loss may now be calculated from

$$\frac{dQ}{dt} = H \left[A_{wr}(T - T_{wr}) + A_{wh}(T - T_{wh}) \right] \qquad (35)$$

where subscript wr refers to the rotor surface and wh to the remaining surfaces. Thus A_{wh} is defined from Eq. 26 as

$$A_{wh} = A - A_{wr} \qquad (36)$$

The housing's wall temperature is estimated by modeling the engine's coolant system as a geometrically equivalent set of tubes. The heat flux measured to the cooling system was then equated to the heat flux driven by the difference between the wall temperature and the mean fluid temperature. The rotor temperatures are based on data of Ref. 13.

The heat loss calculated by Eq. 35 is the heat loss from a system which includes the quench layers. Our analysis divides the region between the flame fronts into a bulk burned gas and an unburned quench layer. The heat transfer from the bulk gas is different from that given by Eq. 35 since a portion of the thermal boundary layer has been removed from our open system model of the burned region. Two limiting cases have been analyzed. The first analysis assumes that the thermal boundary layer and the quench layer are the same thickness, therefore the bulk gas is adiabatic and Q = O in Eq. 17. Since the thermal boundary layer grows with time, it is expected that this assumption will be good early in the combustion phase and break down as time goes on. This expectation leads to the second analysis; assuming that the quench layer is much thinner than the thermal boundary layer so that Q in Eq. 17 is calculated according to Eqs. 35 and 14.

The unburned hydrocarbons in the Wankel exhaust have two primary sources—leakage of unburned fuel and air to the exhausting chamber and incomplete combustion resulting from the flame's failure to propagate to the cold walls or into crevice volumes. The ultimate hydrocarbon concentration in the exhaust depends upon the fraction of unburned hydrocarbons which oxidizes after combustion has ceased (postoxidation) and the fraction which is exhausted, both of which depend upon the oxygen available and are of primary importance for lean running engines (14).

Shortly after the exhaust port opens, unburned fuel and air leak from the combusting chamber to the exhausting chamber according to Eq. 23. After combustion has ceased, at time t*, the leakage is burned gas and does not contribute to the hydrocarbon concentration of the exhaust. The contribution of HC in the exhaust due to leakage is estimated by integrating the unburned leakage. The contribution due to quenching is estimated by integrating Eq. 27 and the contribution due to crevice volumes is estimated from the engine and seal geometry and chamber conditions at the time of quench.

Having established the mass fraction burned as a function of crank angle, predictions of NO may be made using $x(\theta)$ as a

weighting function. The procedure is detailed in Ref. 3, a brief description of which follows.

Lavoie et al. (7) showed that under conditions prevailing in spark ignition engines the process of NO formation is primarily governed by the following reactions:

$$N + NO \rightleftharpoons N_2 + O \qquad (37)$$

$$N + O_2 \rightleftharpoons NO + O \qquad (38)$$

$$N + OH \rightleftharpoons NO + H \qquad (39)$$
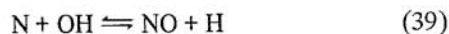
The hydrocarbon oxidation reactions are fast relative to the NO formation process and a reasonable approximation is that the species, O, O_2, H, OH, and N_2, are in equilibrium. Since the N atom mole fraction is of order 10^{-7}, the steady-state approximation is made for [N]. (The brackets denote concentration in g moles/cm^3). Hence the rate of change of NO concentration in a fluid element of volume V is

$$\frac{1}{V}\frac{d[NO]}{dt} = \frac{2[1 - ([NO]/[NO]_e^2)R_1}{(1 + K[NO]/[NO]_e)} \qquad (40)$$

where $R_1 = k_1[N]_e[NO]_e$ is the one-way equilibrium reaction rate of Eq. 37 with subscript e denoting equilibrium concentration, and $K = R_1/(R_2 + R_3)$ with R_2 and R_3 defined analogously to R_1 but for Eqs. 38 and 39.

The kinetic model is coupled to an equilibrium model of the combustion process based on the measured pressure versus time curve. The exhaust concentration is then calculated by integrating across the charge after NO levels are frozen. The integral to be evaluated is

$$[NO]_{ave} = \int_0^1 [NO]_{fr}dx \qquad (41)$$

where $[NO]_{ave}$ is the average concentration in the bulk gas and $[NO]_{fr}$ is the final frozen NO concentration in the element that burned when the mass fraction burned was x.

EXPERIMENTS AND APPARATUS

The modeling and experiments center around a Toyo Kogyo series 10A engine which has been described previously in detail (15). The general characteristics of the engine are detailed in Table 2. The engine, intended for a Mazda automobile, was run as designed; the distributors controlled the spark timing according to engine speed and inlet pressure, and a four barrel carburetor determined the fuel-air ratio (F/A). The engine was lubricated with Texaco URSA oil LA-23 and fueled with iso-octane.

The chamber pressure was recorded with a PCB model 111A24 piezoelectric pressure transducer mounted on the

Table 2 - Toyo Kogyo Engine Specifications

Type	Rotary piston engine, in-line, 2 rotor, water cooled
Displacement	491 cm^3, 2 rotors (29.96 in^3, 2 rotors)
Compression ratio	9.4:1
Compression pressure	6.0 kg/cm^2 (85 psi) at 280 rpm
Max brake horsepower	100 PS/7000 rpm (JIS)
	110 hp/7000 rpm (SAE)
Max torque	13.5 m-kg/3500 rpm (JIS)
	100 ft-lb/4000 rpm (SAE)
Port timing:	
Intake opens	Primary: 32 deg atdc
	Secondary: 32 deg atdc
Intake closes	Primary: 40 deg abdc
	Secondary: 40 deg abdc
Exhaust opens	75 deg bbdc
Exhaust closes	35 deg atdc

leading spark plug. The spark plug adapter provided by PCB is not adequate for accurate pressure measurements since attenuation of the pressure signal apparently occurred. To calibrate the pressure measuring system during running conditions, a series of experiments was performed with a balanced pressure indicator (16) mounted simultaneously in place of the trailing spark. However, the combustion was so adversely affected by the removal of the trailing spark plug that the calibration desired could not be obtained. The calibration of the pressure measuring system was therefore accomplished by forcing the integral of PdV over the cycle to be equal to the average work measured by the dynamometer. The pressure records so obtained are estimated to be accurate to about ±5%. Our crank angle measurements are accurate to ±1 crank angle deg.

To measure the time averaged fuel flow delivered to the engine a Floscan Model 200A electronic totalizer was coupled to a clock. The system measured the time to consume a given mass of fuel to an accuracy better than 1/2%.

The exhaust gas analysis was done with the following instruments: TECO Model 10 Chemiluminescent NO analyzer, Beckman Model 315A CO and CO_2 analyzers, Beckman Model 777 lab O_2 analyzer, and a Scott Model 215 heated total HC analyzer. With the exception of the HC, all measurements were made on a dry basis; the HC analyzer requires no sample conditioning.

Airflow into the engine is determined from the F/A calculated from exhaust gas analysis (17) and fuel flow measurements. At high airflows a redundant measurement was made with an ASME square-edged orifice mounted upstream of the carburetor. At low flow rates the orifice system failed because leakage of air through the carburetor was a significant fraction of the total flow.

The data analyzed come from three of the power curves shown in Fig. 4. Also shown is Toyo Kogyo's measured curve for the series 10A engine. Throughout the paper reference will be made to low, middle, and maximum bmep, indicating these power curves.
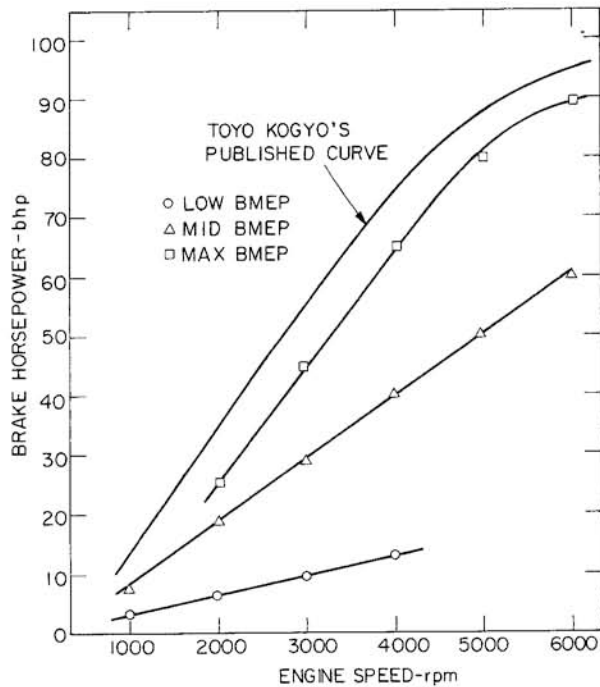
Fig. 4 - Experimental power curves and Toyo Kogyo's specified performance curve for the series 10A engine

Table 3 - Major Engine Operating Parameters

Engine Speed, rpm	bmep, psi	fmep, psi	Leading Spark, deg btdc	Trailing Spark, deg btdc	Front Rotor CO, %	ϕ	Rear Rotor CO, %	ϕ
2000	18	24	−44	−46	2.2	1.05	−	−
3000	21	29	−45	−45	2.2	1.03	−	−
4000	22	30	−44	−44	2.5	1.02	1.5	0.99
2000	63	24	−27	−14	1.9	1.02	1.3	0.99
3000	63	28	−29	−20	1.9	1.03	1.9	1.03
4000	62	30	−31	−25	3.9	1.11	3.4	1.09
5000	67	33	−27	−20	4.7	1.15	4.5	1.14
2000	85	24	−20	−12	6.3	1.24	6.8	1.26
3000	96	27	−23	−10	8.2	1.30	8.5	1.32
4000	106	30	−23	− 9	7.5	1.26	6.8	1.24
5000	103	34	−24	−10	6.2	1.22	6.3	1.21

Table 4 - Mass Balance from Ignition to End of Combustion

Engine Speed, rpm	Load	m_o, 10^{-3}kg	m_q/m_o, %	m_L/m_o, %	m_{cv}/m_o, %	m_b/m_o, %
2000	Low	3.1	4.9	7.3	0.6	87
3000	Low	2.6	5.2	5.0	0.7	89
4000	Low	2.6	5.8	3.5	0.7	90
2000	Mid	5.2	3.9	6.4	0.5	89
3000	Mid	4.6	4.2	5.0	0.6	90
4000	Mid	4.2	3.4	4.0	0.7	92
5000	Mid	4.3	3.1	3.1	0.6	93
2000	Max	5.8	2.5	6.1	0.5	91
3000	Max	5.8	2.4	4.1	0.6	93
4000	Max	5.7	2.6	3.2	0.6	94
5000	Max	5.6	2.7	2.5	0.6	94

Note:

m_o = mass in chamber at ignition

m_q = mass in quench layers

m_L = mass which leaked out of chamber

m_{cv} = mass in crevice volumes

m_b = mass burned during combustion

The total mass in the chamber at the time combustion ends is
$m_b + m_{cv} + m_q = m_o - m_L$.

RESULTS AND DISCUSSION

Implicit in our analysis is the assumption that the engine is symmetrical, that is, the same amounts of fuel and air are delivered to each rotor and that each rotor has the same thermal efficiency. Table 3 gives values of major engine operating parameters. The table shows carbon monoxide and equivalence ratio taken from the exhaust of the front rear rotors as an indication of the engine's symmetry. All analysis has been performed on data of the front rotor.

Using the model already described, curves of mass fraction burned as a function of crank angle were calculated from the measured chamber pressure versus time data. Results for low bmep, mid bmep, and max bmep for a range of engine speeds are shown in Figs. 5, 6, and 7, respectively. Two sets of curves are shown for each engine load. The curves on the right were calculated assuming the bulk gas in Fig. 3 was adiabatic. This corresponds to the assumption that during combustion, the thickness of the quench layer and the thermal boundary layer are comparable in magnitude. The curves on the left were calculated assuming heat loss of the bulk gas is given by Eq. 35. This corresponds to the assumption that the quench layer thickness is much less than the thermal boundary layer thickness during combustion.

When x = 1, all the unburned gas available for combustion has been burned. The unburned gas not available for combustion has either been leaked out of the combusting chamber or lies in the quench layers and crevice volumes. Only half the leakage is truly wasted, since half of the leakage out of the combusting chamber is into the compressing chamber where it may become available for the next combustion process. Table 4 shows a mass balance performed on the combustion chamber

from ignition until the end of combustion. Shown are the relative proportions of the mass not available for combustion and the total mass which was burned.

An examination of the mass fraction burned curves reveals that x_{max} = 1 lies between the limiting cases analyzed. Thus, within the accuracy of our model and experimental uncertainty, all the mass has been accounted for, and we conclude that the manner in which the model handles heat transfer from the bulk gas is important.

The burned mass fraction curves also qualitatively describe the combustion process. It can be seen that the interval from the angle of ignition to the end of combustion is on the order
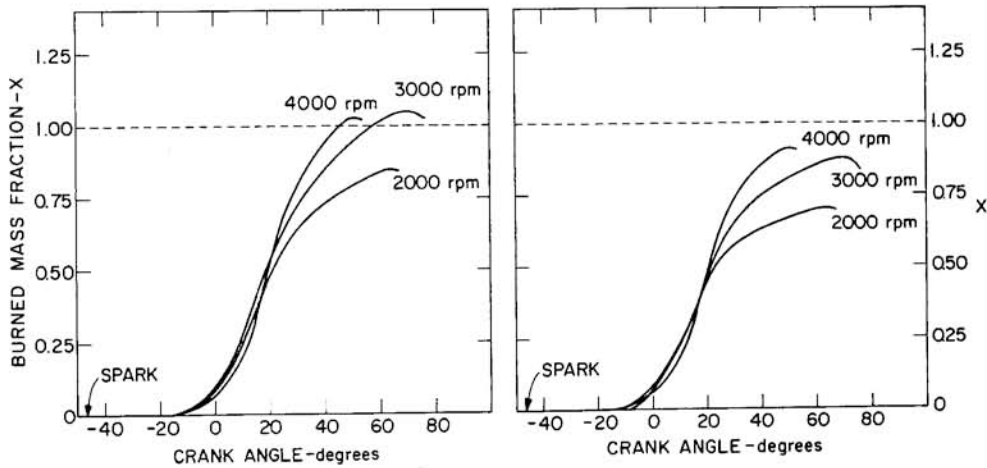
Fig. 5 - Mass fraction burned as a function of crank angle calculated from low bmep experiments: Left–Nonadiabatic burned gas, Right–Adiabatic burned gas
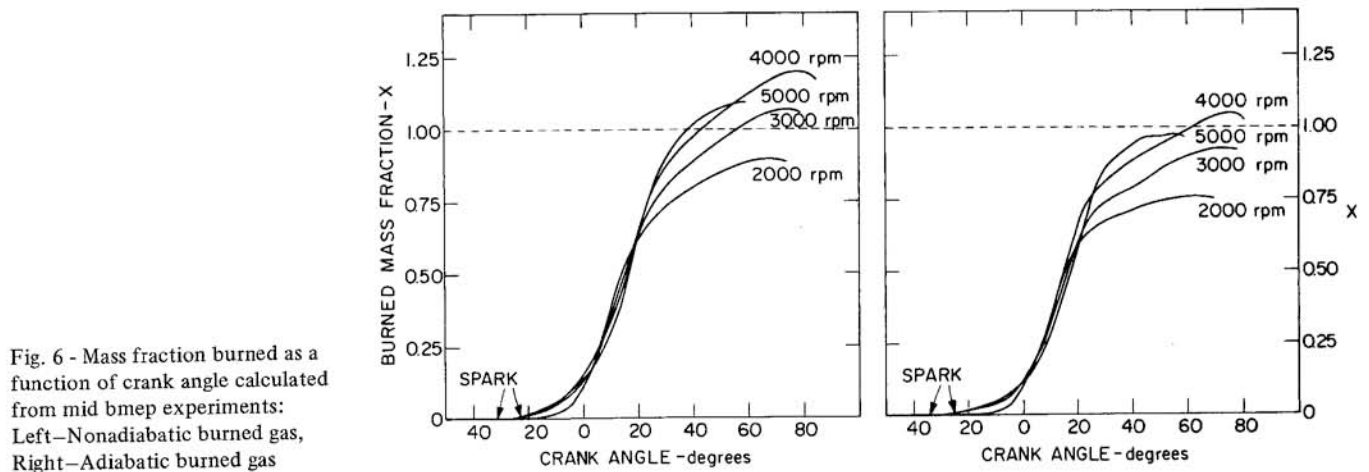

Fig. 6 - Mass fraction burned as a function of crank angle calculated from mid bmep experiments: Left–Nonadiabatic burned gas, Right–Adiabatic burned gas
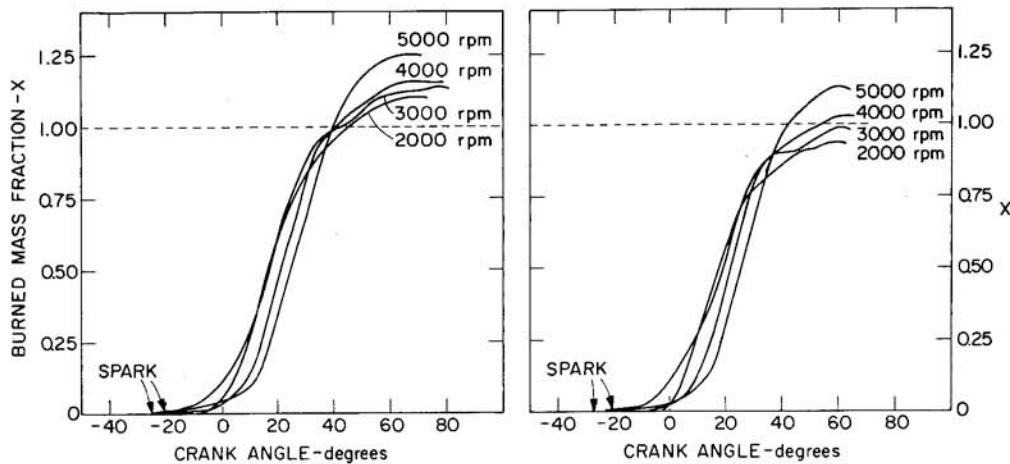

Fig. 7 - Mass fraction burned as a function of crank angle calculated from max bmep experiments: Left–Nonadiabatic burned gas, Right–Adiabatic burned gas

of 90 crank angle deg. Ignition delay, the angle between ignition and the time when, say, $x = 0.1$, is a function of engine loading, and is about 30 deg at low bmep and 5-10 deg at max bmep. This apparent ignition delay behavior with engine load is consistent with experimental observations of the cycle to cycle variation of peak pressure.

Heat losses in the engine were measured as the heat rejected to the water and oil coolant systems corrected for frictional heating of the oil. The frictional heating of the oil was mea-

sured in a motored engine and is approximately 1 kW/1000 rpm. Fig. 8 compares the calculated average heat loss to the chamber walls (filled symbols) with the average measured heat loss (open symbols). The agreement shows that our model predicts an acceptable average heat transfer coefficient. At tdc, however, the local heat transfer coefficient may exceed the average by as much as a factor of 3 (see Appendix A) due to high local gas velocities.

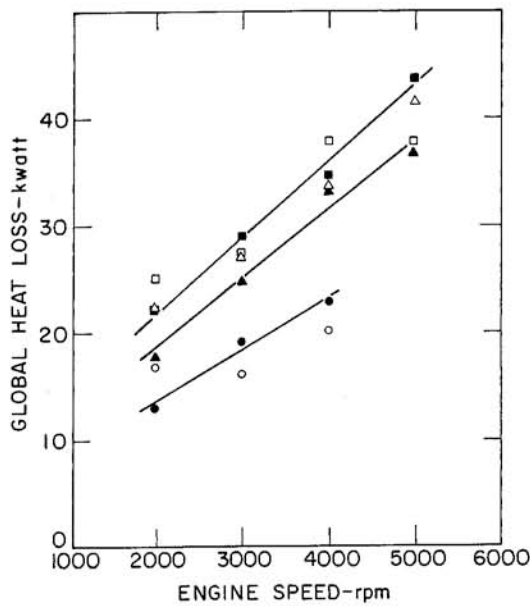The hydrocarbon model described predicts the total mass

Fig. 8 - Comparison of measured global heat loss (open symbols) to predicted average heat loss (filled symbols); ○ = low bmep, △ = mid bmep, □ = max bmep

Table 5 - Mass Balance from Time Intake Port Closed Until
Exhaust Port is About to Open

Engine Speed, rpm	Load	m_{ic}, 10^{-3}kg	m_u/m_{ic}, %	m_B/m_{ic}, %	m/m_{ic}, %
2000	Low	3.2	8.5	0.8	91
3000	Low	2.7	5.9	1.1	93
4000	Low	2.6	4.2	0.8	96
2000	Mid	5.3	8.5	1.7	90
3000	Mid	4.6	6.3	1.1	93
4000	Mid	4.2	5.0	1.0	94
5000	Mid	4.3	3.7	0.8	96
2000	Max	5.9	8.4	2.4	89
3000	Max	5.8	5.7	1.6	93
4000	Max	5.7	4.2	1.2	95
5000	Max	5.6	3.3	1.1	96

Note:

m_{ic} = mass in chamber when intake port closed

m_u = net mass which left as unburned gas (1/2 goes into exhaust)

m_B = net mass which left as burned gas

m = mass in chamber when expansion ends

of unburned hydrocarbons that can be expected to form within the engine. Table 5 is a mass balance performed on a chamber from the time the intake port closes until the exhaust port is about to open. Let us refer to that chamber as the central chamber. As the central chamber begins compression unburned gas leaks to the trailing chamber (inducting)* and burned gas leaks in from the leading chamber (expanding). A short time later the exhaust port is uncovered in the leading chamber and unburned gas begins to leak from the central chamber to the leading chamber (exhausting) and continues until the central chamber has burned all the mass available for combustion; the integral of this leakage to the exhaust is the leakage contribution to HC in the exhaust. Also during the compression and combustion phases of the central chamber, leakage of unburned gas continues to leak to the trailing chamber which has been inducting. Once burning has been completed in the central chamber the leakage out to the trailing and leading chambers becomes burned gas. This burned gas leaked to the trailing chamber contributes to the effective residual mass fraction defined by Eq. 25. The reason that the unburned gas which leaked from the central chamber to the trailing chamber prior to combustion's end does not affect the effective residual mass fraction is because it is already of the same composition that the trailing chamber will be when it becomes the combusting chamber. As expansion continues, the central chamber leaks burned gas to both the leading and trail-

*For a brief time at the start of compression the trailing chamber is at the end of the exhaust process. The direction and composition of leakage past the apex seal during this period are a function of engine load. The model takes into account this behavior and shows it insignificant; thus it is omitted from the discussion.

ing chambers until the exhaust port opens. Table 5 shows the net unburned mass and burned mass which left the central chamber, the unburned leakage from the central chamber to the exhaust, and the mass in chamber just prior to the exhaust process.

If subsequent HC oxidation is small (as would be expected since the engine operates fuel-rich (14)) and the HC is exhausted in the same proportion as the burned gas (an assumption supported by experiments now in progress), the data in Table 5 can be used to estimate the HC emissions. Our experiments measured HC with a flame ionization detector (FID) and our calculations have been converted to the equivalent ppmC reading. Denoting the mass of unburned gas in the exhaust due to leakage, quenching, and crevice volumes as m_{HC} the equivalent ppmC concentration is

$$[HC] = \frac{8}{114} \frac{m_{HC}(1-\epsilon)^2}{m_{int}} \frac{M_e \phi \cdot 10^6}{(15+\phi)}, ppmC \quad (42)$$

where:

M_e = molecular weight of exhaust

ϕ = equivalence ratio

where the unburned gas is assumed to consist of isooctane (C_8H_{18}) and air mixed in the same proportions as the inlet charge. The term $(1-\epsilon)^2$ accounts for the fraction assumed exhausted and the fraction of burned gas in the unburned gas defined by Eq. 25.

Exhaust concentrations of unburned HC predicted and measured are shown in Figs. 9-11 as functions of reciprocal engine
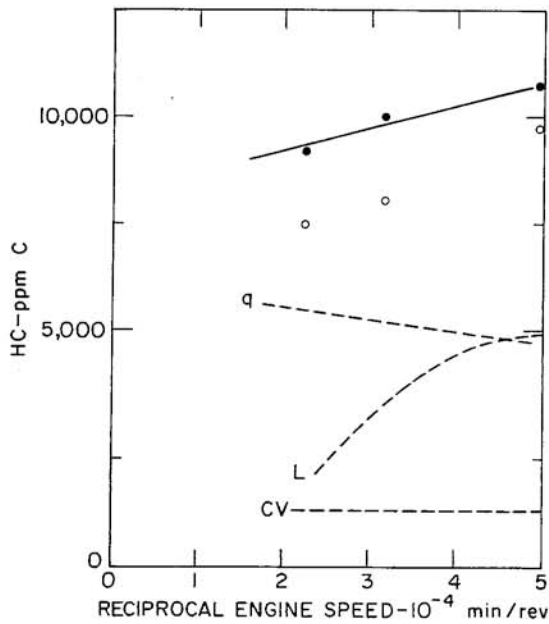
Fig. 9 - Measured HC (open symbols) and calculated HC (filled symbols) as functions of reciprocal engine speed. Dashed lines q, L, and CV show calculated proportions of HC due to quenching, leakage, and crevice volumes, respectively (low bmep)
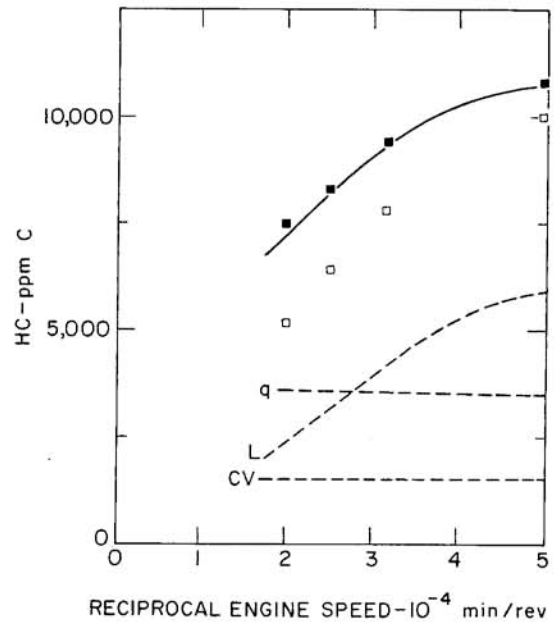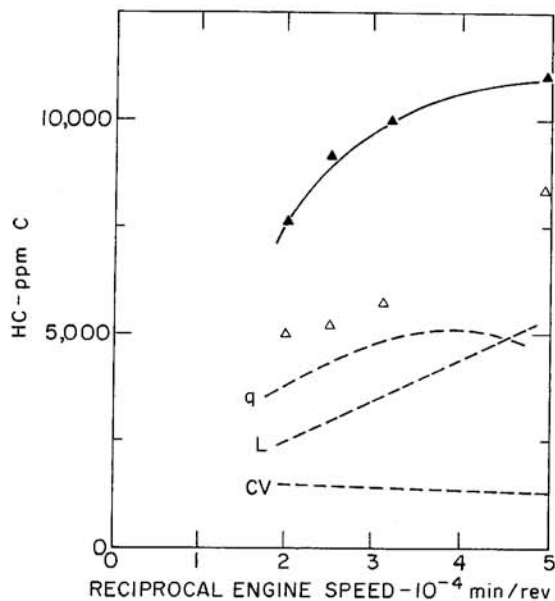

Fig. 11 - Measured HC (open symbols) and calculated HC (filled symbols) as functions of reciprocal engine speed. Dashed lines q, L, and CV show the calculated proportions of HC due to quenching, leakage, and crevice volumes, respectively (max bmep)

Fig. 10 - Measured HC (open symbols) and calculated HC (filled symbols) as functions of reciprocal engine speed. Dashed lines q, L, and CV show the calculated proportions of HC due to quenching, leakage, and crevice volumes, respectively (mid bmep)

speed. The experimental data show a strong dependence of HC on engine speed, almost linearly with reciprocal engine speed. This is an indication of the relative importance of leakage as a source of HC. The predicted HC are higher than those measured, but are of the correct order of magnitude and show the correct speed dependence. Thus, conclusions may be drawn as to the nature of the Wankel's HC characteristics.

The curves labeled q, L, and CV in Figs. 9-11 are the calcu-

lated contributions to the total HC concentration of the three sources: quenching, leakage, and crevice volumes. At high speed the quenched HC are the dominant source, whereas at low speeds the leakage source dominates. The transition from quenching to leakage as the most important source occurs at about 2000 rpm for light engine loads, and at about 3500 rpm for WOT, max bmep. In all cases the crevice volume contribution is constant at about 1500 ppmC.

The thermal efficiency, defined as the ratio of the useful work obtained to the heat that would be released by all of the fuel delivered to the engine, is also tabulated in Table 5. The thermal efficiency appears to be lower than that of an equivalent piston engine. For example, a CFR running at a compression ratio of 9.4:1 at WOT typically has an efficiency of 23% (Ref. 1, p. 67). Table 4 shows mass of unburned gas which ends up in the exhaust due to leakage. Table 3 shows the quenching and crevice volume contributions. Roughly 10% of the fuel the Wankel receives is never used, it leaves the engine in the exhaust.

The NO calculations are illustrated in Fig. 12. The calculation of the mass fraction burned curve $x(\theta)$ from the measured chamber pressure—time curve $p(\theta)$ has already been described. A set of elements on the $x(\theta)$ curve spaced between $x = 0$ and $x = 1$ are chosen. The enthalpy of each element at time of combustion is computed. An equilibrium thermodynamic program is used to calculate the burned gas temperature, and O, OH, H, O_2 species equilibrium concentrations for each element, as a function of time, from the unburned mixture enthalpy at time of combustion along an isentrope following the pressure-time curve (3). The NO concentration is calculated along this state-time path using Eq. 40. It is thus assumed that each element is in the core gas (that is, outside the
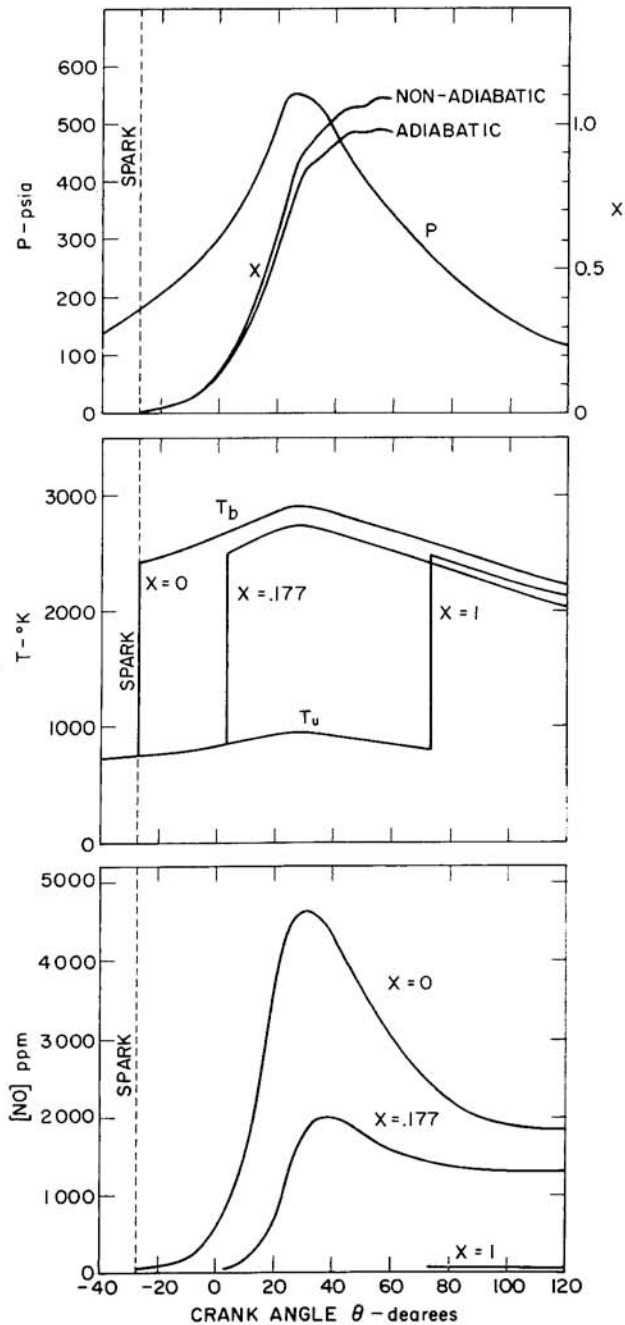
Fig. 12 - Top, measured pressure p and calculated mass fraction burned (x) as function of crank angle (θ). Center, equilibrium calculations of burned and unburned gas temperatures T_b and T_u as function of θ. Bottom, NO mass fraction as function of crank angle for elements which burn at different times. All curves refer to 5000 rpm, mid bmep

Table 6 - Comparison of Measured Nitric Oxide ([NO]$_m$) to Predicted Nitric Oxide ([NO]$_p$) Exhaust Concentrations

Engine Speed, rpm	bmep	[NO]$_m$, ppm	[NO]$_p$, ppm	NO_p/NO_m	$\frac{T_a - T_{na}}{T_{na}}$, %	$\frac{Q}{m}$, kJ/g
2000	Low	190	1700	8.7	6.3	0.75
3000	Low	340	2200	6.5	6.0	0.74
4000	Low	190	1500	8.0	4.7	0.64
2000	Mid	1050	2800	2.6	4.0	0.64
3000	Mid	1100	2700	2.5	4.6	0.70
4000	Mid	850	1500	1.7	4.1	0.75
5000	Mid	500	880	1.8	4.2	0.51
2000	Max	180	340	1.9	4.2	0.67
3000	Max	100	230	2.3	4.4	0.58
4000	Max	200	340	1.7	4.1	0.53
5000	Max	325	550	1.7	0.0	0.45

the bulk gas after NO levels have frozen ($\theta = 120$ deg) according to Eq. 40. From a knowledge of the mass of the bulk gas, the total mass of NO formed is determined.

Assuming that the NO formed is exhausted in the same proportions as the burned gas, the average concentration of NO in the exhaust may be determined.

$$[NO] = \frac{[NO]_{ave}}{(1 - [H_2O]_e)} \frac{m_{bulk}}{m_{int}} (1 - \epsilon) M_e \cdot 10^6, \text{ ppm} \tag{43}$$

The exhaust equilibrium concentration of water $[H_2O]_e$ corrects the prediction to a dry basis for comparison to experimental data.

Table 6 compares the predicted NO exhaust concentrations with the measured values. At mid and max bmep, agreement to within about a factor of 2 is obtained. Due to uncertainties in the chamber pressure-time measurements, and limitations in the actual thermodynamic and kinetic models, a more accurate prediction of the actual magnitude should not be expected. In contrast, at low bmep, the predictions are almost an order of magnitude above the measurements.

In similar calculations for piston engines (18, 19) it has been shown that an error of 5% in burned gas temperatures gives almost a factor of 2 error in the prediction of NO at $\phi = 1.0$. The sensitivity of the calculations to temperature errors decreases as the equivalence ratio increases above 1.0 (3).

The calculations made from the low bmep conditions distinguished themselves in that extraordinarily high frozen levels of NO were achieved in the elements which burned very early in the combustion process. These elements burn in the region of tdc where we can expect the heat transfer coefficient to be as much as three times higher than that predicted by Eq. 35 (see Appendix A). The calculated equilibrium temperatures used in the NO predictions were made on the assumption that the mass of burned gas in the thermal boundary layers was

thermal boundary layer), and that mixing between different gas elements can be neglected.

The temperature histories of three elements which burn at different times are shown in the center of Fig. 12. The corresponding NO concentrations in these elements are shown at the bottom of Fig. 12. With the burned mass fraction versus angle known from the perfect gas model of combustion, the average concentration in the bulk gas is calculated by integrating across

small compared with the mass in the core flow which was compressed and expanded isentropically. While this assumption appeared to be satisfactory for reciprocating spark-ignition engines (3, 19), the above discussion indicates that it may well not be satisfactory for Wankel engines. A more careful analysis of the boundary layer structure in a Wankel engine is in order.

Table 6 indicates why the NO calculations are more sensitive to the isentropic core gas assumption at low bmep. T_a is the peak average bulk burned gas temperature from the perfect gas performance model incorporating an adiabatic bulk gas, while T_{na} is a calculated nonadiabatic model and corresponds to a uniform heat loss from the bulk gas. Also shown is the integrated heat loss per unit mass during the combustion phase. The heat transfer per unit mass is larger at lower bmep and in the nonadiabatic calculations the peak temperature occurred earlier in the cycle than in the adiabatic analysis. Reference to Table 2 shows that at low bmep the engine runs closer to stoichiometric and runs progressively richer as the load increases. We may conclude that temperature errors due to inadequacies in the thermal boundary layer model would be greater at light load and thus the effect on NO predictions more important than at high load.

It has been suggested that mixture nonuniformities inside the chamber significantly affect the NO emission characteristics. From our study we have no evidence which pertains to this question. This is also an area for additional study.

The estimated residual mass fraction defined by Eq. 25 is shown tabulated in Table 7. Note that the effective residual mass fraction is of the same order as the residual mass fraction typical of piston engines. Based on these observations we may conclude the lower NO emissions of the Wankel are not due to an internal exhaust gas recirculation.

CONCLUSIONS

1. A Wankel engine performance model has been developed which is able to predict the mass in any chamber at any given time. The model incorporates global heat transfer, flame quenching, and gas leakage, and successfully predicts the mass of gas burned as a function of crank angle from a measured pressure-time diagram.

2. The model also successfully predicts unburned hydrocarbon emissions. Quenching is the dominant source of HC at high speeds and leakage dominates at low speeds. The transition occurs at about 2500 rpm. The crevice volume contribution is a secondary source independent of speed and load.

3. NO predictions were made by coupling this performance model with a previously developed kinetic model of NO formation. Predictions were about a factor of 2 higher than measurements at mid and high bmep, but were about a factor of 7 higher at low bmep. It is believed that inadequate modeling of the effect of heat transfer on burned gas temperatures is the probable cause of the discrepancy at light loads.

4. This discrepancy in NO predictions at light load, and our analysis of motored pressure-time curves which suggests that heat transfer at tdc may be a factor of 3 higher than is indicated by the global model, indicates that the boundary layer structure and bulk fluid mechanics in the Wankel engine must be examined in more detail than has been found necessary to date in reciprocating engines.

Table 7 - Residual Mass Fraction and Measured Thermal Efficiency

Engine Speed, rpm	bmep	Residual Mass Fraction, %	Thermal Efficiency, %
2000	Low	10	7.6
3000	Low	11	11.2
4000	Low	11	12.0
2000	Mid	7	16.3
3000	Mid	7	18.4
4000	Mid	7	18.3
5000	Mid	8	18.4
2000	Max	6	16.3
3000	Max	6	17.2
4000	Max	6	18.3
5000	Max	6	20.4

REFERENCES

1. J. B. Heywood and J. C. Keck, "Formation of Hydrocarbons and Oxides of Nitrogen in Automobile Engines." Environmental Science & Technology, Vol. 7 (1973), pp. 216-223.

2. D. J. Patterson and N. A. Henein, "Emissions from Combustion Engines and Their Control." Michigan: Ann Arbor Science Publishers, Inc., 1972.

3. K. Komiyama and J. B. Heywood, "Predicting NO_x Emissions and Effects of Exhaust Gas Recirculation in Spark-Ignition Engines." Paper 730475 presented at SAE Automobile Engineering Meeting, Detroit, May 1973.

4. R. F. Ansdale, "The Wankel RC Engine." ILIFFE, London, 1968.

5. F. V. Bracco and W. A. Sirignano, "Theoretical Analysis of Wankel Engine Combustion." Combustion Science and Technology, Vol. 7 (1973), pp. 109-123.

6. M. K. Eberle and E. D. Klomp, "An Evaluation of the Potential Performance Gain from Leakage Reduction in Rotary Engines." Paper 730117 presented at SAE Automotive Engineering Congress, Detroit, January 1973.

7. G. A. Lavoie, J. B. Heywood, and J. C. Keck, "Experimental and Theoretical Study of Nitric Oxide Formation in Internal Combustion Engines." Combustion Science and Technology, Vol. 1 (1970), pp. 313-326.

8. R. Friedman and W. C. Johnston, "Pressure Depen-

dence of Quenching Distance of Normal Heptane, Iso-Octane, Benzene, and Ethyl Ether Flames." Jrl. of Chemical Physics, Vol. 20 (1952), pp. 919-920.

9. J. T. Agnew and K. A. Green, "Quenching Distances of Propane-Air Flames in a Constant-Volume Bomb." Combustion and Flame, Vol. 15 (1970), pp. 189-191.

10. R. Friedman and W. C. Johnston, "The Wall-Quenching of Laminar Propane Flames as a Function of Pressure, Temperature, and Air-Fuel Ratio." Jrl. Applied Physics, Vol. 21 (1950), pp. 791-795.

11. J. M. Ellenberger and D. A. Bowlus, "Single Wall Quench Distance Measurements." Presented at the 1971 Technical Session, Central States Section. Combustion Institute, March 1971.

12. G. Woschni, "A Universally Applicable Equation for the Instantaneous Heat Transfer Coefficient in the Internal Combustion Engine." SAE Transactions, Vol. 76, paper 670931.

13. K. Yamamoto, "Rotary Engine." Toyo Kogyo, Japan, 1969.

14. W. A. Daniel, "Why Engine Variables Affect Exhaust Hydrocarbon Emission." SAE Transactions, Vol. 79 (1970), paper 700108.

15. K. Yamamoto and T. Kuroda, "Toyo Kogyo's Research and Development on Major Rotary Engine Problems." SAE Transactions, Vol. 79 (1970), paper 700079.

16. C. F. Taylor and E. S. Taylor, "The Internal Combustion Engine." Philadelphia: International Textbook, 1961.

17. R. S. Spindt, "Air-Fuel Ratios from Exhaust Gas Analysis." SAE Transactions, Vol. 74 (1965), paper 650507.

18. J. B. Heywood, S. M. Mathews, and B. Owen, "Predictions of Nitric Oxide Concentrations in a Spark-Ignition Engine Compared with Exhaust Measurements." Paper 710011 presented at SAE Automotive Engineering Congress, Detroit, January 1971.

19. P. Blumberg and J. T. Kummer, "Prediction of NO Formation in Spark-Ignited Engines—An Analysis of Methods of Control." Combustion Science and Technology, October 1971.

APPENDIX A

LEAKAGE AREA

Eberle and Klomp (6), using the same type engine we do, conclude that the effective leakage area per chamber is approximately 2 mm^2. They also suggest that side seal leakage is about 1/4-1/3 of the total leakage. Our measurements of static clearances between corner seal, apex seal, and side covers indicate that at engine operating temperature the leakage area is of order 1 mm^2.

In principle, we can determine the effective area from motoring pressure versus time diagrams. Since the working fluid during motoring is air and involves no combustion, uncertainties in the modeling to predict the effective area are minimized. In the region of tdc the leakage out of the chamber is described by Eq. 23. Combining Eqs. 1, 19, and 23, the leakage area may be determined at tdc as

$$C_d A = \frac{\left[\dfrac{(\gamma - 1)}{P} \dfrac{dQ}{dt} \dfrac{d(\ell n P V^\gamma)}{dt}\right]}{\sqrt{\gamma R T} \left(\dfrac{2}{\gamma + 1}\right)^{(\gamma + 1)/2(\gamma - 1)}} \qquad (A\text{-}1)$$

Fig. A-1 is a plot of $\ell n P V^\gamma$ for two different pressure measurements of the same event. The curve labeled BPI was measured by the balanced pressure indicator while the PCB curve is from a piezoelectric transducer. The data are for the engine being run at 3000 rpm WOT. Our analysis of these curves to de-
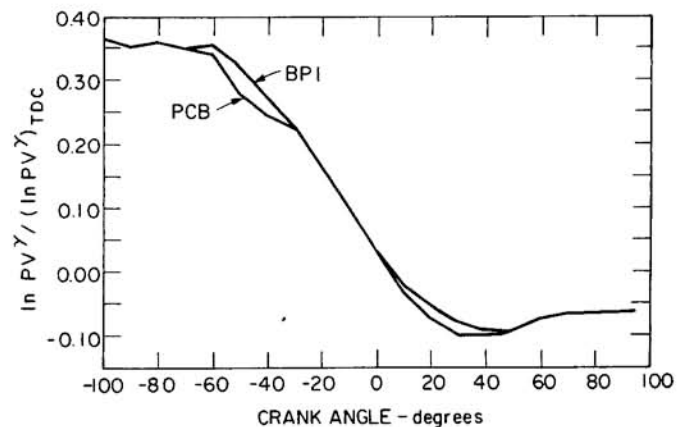

Fig. A-1 - $\ell n P V^\gamma$ with respect to tdc for engine motored at 3000 rpm WOT versus crank angle. BPI curve represents measurements made with balanced pressure indicator while PCB curve represents measurements made with piezoelectric transducer

termine $C_d A$ leads to the following conclusions. Using the curves in Fig. A-1 and our estimate of the local heat transfer from Eq. 35 we calculate an area which is an order of magnitude larger than the geometrically determined value. We have therefore concluded that our instantaneous heat transfer coefficient is too low in the region of tdc by a significant factor. That this is so can be seen from Ref. 15, where the local gas velocity distribution due to geometric motion of the rotor is

shown. Instantaneously the velocity may at some position be three times the velocity described by Eq. 30. This is because at tdc the gas near the trailing apex is still being compressed while the gas near the leading apex is expanding; thus establishing a flow from the trailing part of the chamber to the leading part of the chamber.

Throughout this paper calculations are based on an effective leakage area of 1 mm^2 per chamber which was determined geometrically, and not from motored pressure-time curves as had originally been intended. This leakage area used in the performance model gives satisfactory predictions of mass fraction burned and leakage HC emissions.

APPENDIX B

The thermodynamic properties used for the perfect gas models of the burned and unburned gas in the engine performance model are determined from the best fit to equilibrium calculations of thermodynamic properties over the temperature range of interest. Straight lines fitted to equilibrium enthalpy-temperature plots for the appropriate fuel and F/A give slopes equal to C_p in Eq. 4. The intercept at T = 0 K defines the enthalpy of formation. An average molecular weight over the temperature range of interest establishes the gas constant R. The constants γ and C_v are then also defined.

The temperature range used in this procedure for this study for the burned gases is

$$2400 \text{ K} > T_b > 2000 \text{ K} \qquad (B-1)$$

and for the unburned gas

$$800 \text{ K} > T_u > 600 \text{ K} \qquad (B-2)$$
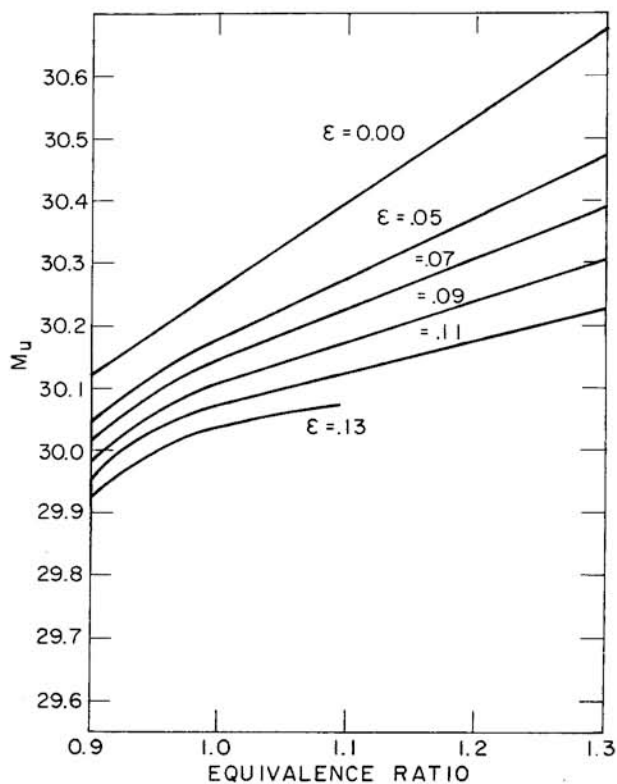
Figs. B-1 - B-5 depict the results.

Fig. B-1 - Molecular weight M_u of unburned gas and burned iso-octane-air-burned gas mixture. ϵ is defined by Eq. 25
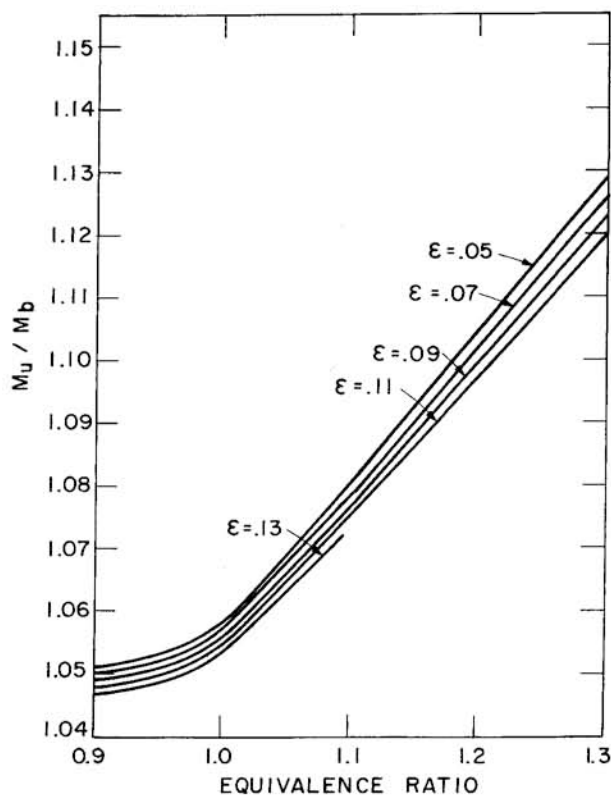

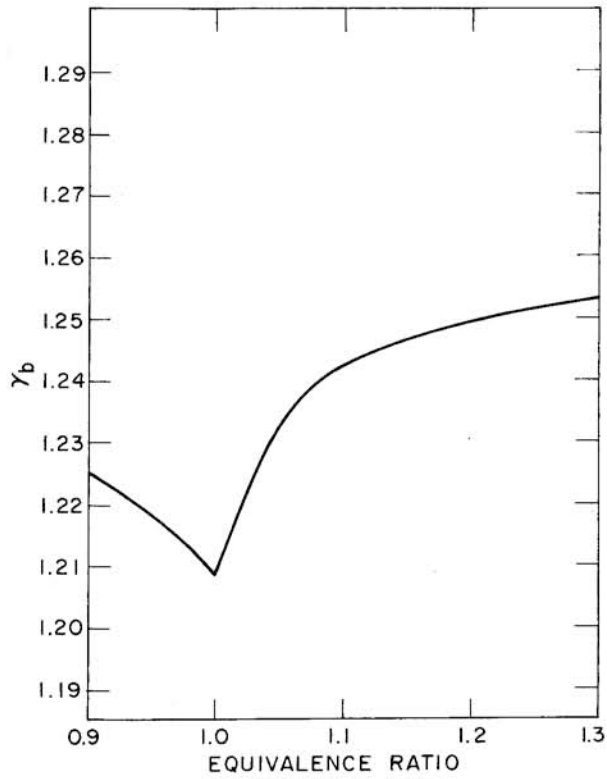Fig. B-2 - Ratio of molecular weight of unburned gas to burned gas, M_u/M_b. ϵ is defined by Eq. 25
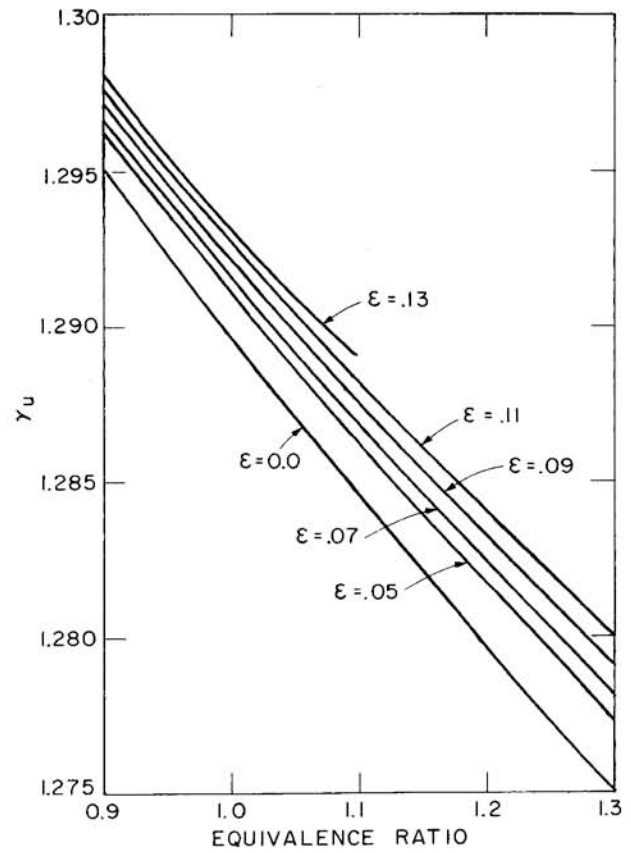
Fig. B-3 - Ratio of specific heats of burned gas γ_b
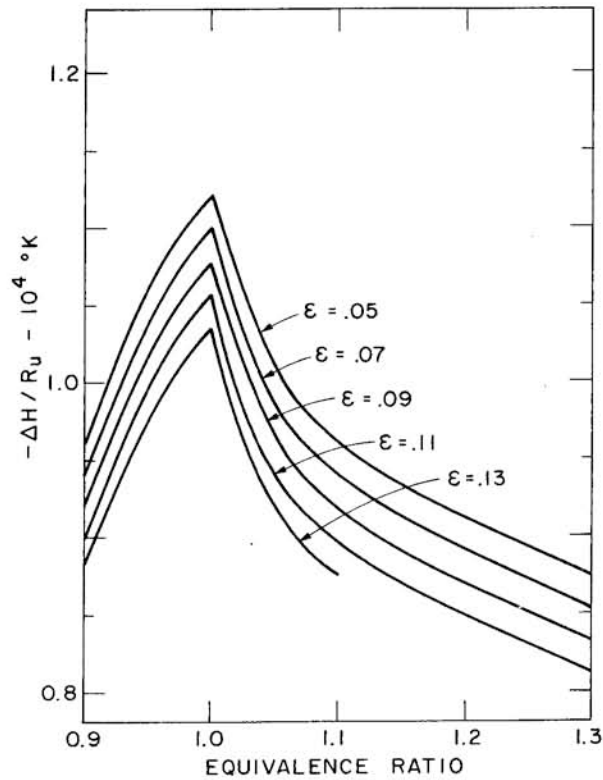

Fig. B-4 - Ratio of specific heats of unburned gas, γ_u. ϵ is defined by
Eq. 25

Fig. B-5 - Ratio $-\Delta H/R_u$ where ΔH is defined by Eq. B-1 and ϵ by
Eq. 25